FPGA-Accelerated Distributed Sensing System for Real-Time Industrial Laser Absorption Spectroscopy Tomography at Kilo-Hertz

FPGA-Accelerated Distributed Sensing System for Real-Time Industrial Laser Absorption Spectroscopy Tomography at Kilo-Hertz

Jiangnan Xia, Godwin Enemali, *Member, IEEE*, Rui Zhang, Yalei Fu, Hugh McCann, Bin Zhou, and Chang Liu, *Senior Member, IEEE*

***Abstract*— Fast and continuous data acquisition (DAQ) with well resolved spectral information is essential for high-speed and high-fidelity measurement of thermophysical parameters of industrial processes using laser absorption spectroscopy tomography (LAST). However, the state-of-the-art DAQ systems suffer a) inability to collect raw spectral data in real time due to the very high data throughput; b) degradation of spectral integrity when excessive on-chip down-sampling is implemented to reduce data throughput. In this work, we designed a star-networked and reconfigurable DAQ system for real-time LAST imaging at kilo-Hz frame rate. The DAQ system is embedded with a new field programmable gate array (FPGA)-accelerated digital lock-in (DLI) technique, whereby a cascaded integrator-comb (CIC) filter is implemented for down-sampling of the raw signal with well-maintained spectral information. Furthermore, a customized data-encapsulation protocol is developed to enable continuity of real-time data communication between the front-end DAQ hubs and back-end processor. Performance of the developed DAQ system is experimentally validated by flame temperature imaging at 1 kHz, providing the necessary temporal resolution to penetrate turbulent flow and related industrial processes such as reaction propagation.**

***Index Terms*— real-time data acquisition; networked embedded system; field programmable gate array; hardware acceleration; laser absorption spectroscopy**

NOMENCLATURE

Acronym	Abbreviation
DAQ	Data Acquisition
LAST	Laser Absorption Spectroscopy Tomography
FPGA	Field Programmable Gate Array
DLIA	Digital Lock-in Amplifier
CIC	Cascaded Integrator-Comb
IPT	Industrial Process Tomography
SNR	Signal-to-Noise Ratio
WMS	Wavelength Modulation Spectroscopy
ADC	Analog-to-Digital Converter
SSM	Semi-Scan Multiplexing
FDM	Frequency-Division Multiplexed
FIR	Finite-Impulse-Response
LPF	Low Pass Filter
UDP	User Datagram Protocol
FIFO	First in, First Out
TS	Time Stamp
FFT	Fast Fourier Transform

Manuscript received November 23, 2022; revised June 14, 2023; accepted June 28, 2023. This work was supported in part by the UK Engineering and Physical Sciences Research Council (Platform Grant EP/P001661/1 and Programme Grant EP/T012595/1). (Corresponding author: Chang Liu).

J. Xia, G. Enemali, R. Zhang, Y. Fu, H. McCann and C. Liu are with the School of Engineering, University of Edinburgh, Edinburgh, EH9 3JL, U.K. (e-mail: C.Liu@ed.ac.uk).

B. Zhou is with the School of Energy and Environment, Southeast University, Nanjing 210018, China.

I. INTRODUCTION

HIGH-speed and high-fidelity distributed sensing networks and data acquisition (DAQ) systems are essential for monitoring and control of industrial process [1]–[3]. To comprehensively characterize the industrial processes, industrial process tomography (IPT) techniques have been widely developed for acquiring two/three-dimensionally distributed parameters [4]. Depending on different sensing modalities, the IPT techniques generally involve ultra-sensitive measurement of multi-channel electrical [5], ultrasonic [6], optical signals [7], via signal modulation/demodulation techniques to improve the measurement Signal-to-Noise Ratio (SNR). Furthermore, most IPT applications require continuous imaging of the industrial processes with penetrating temporal resolution, placing significant requirement on the high-speed DAQ and real-time data communication between the front-end sensors and back-end high-level processors.

Among the various IPT techniques, laser absorption spectroscopy tomography (LAST) [8], [9] provides the unique capability of imaging thermophysical parameters of reactive flows, e.g., temperature, species concentration and velocity. The implementation of modulation/demodulation technique in LAST is Wavelength Modulation Spectroscopy (WMS) [9], [10]. In WMS, the laser source is driven by the superposition of a low-frequency wavelength scan, f_s, typically from several Hz to a few kHz, and a high-frequency modulation, f_m, typically from 50 kHz to 250 kHz. A faster laser wavelength scan and modulation contribute to higher temporal resolution and stronger measurement noise immunity, respectively. A LAST system with both frequencies at relatively high values

could facilitate dynamic and in-depth characterization of the reactive turbulences, which is highly attractive to the process industry [11]. However, a DAQ system that can sample such laser transmissions from many channels, generally more than 30, is fundamentally and practically challenging due to:

(1) the massive amount of raw digitized data for keeping spectral information;

(2) the highly demanded synchrony and consistency between the sampling channels for snapshotting the target flows;

(3) the high-bandwidth data throughput for real-time front/back-end data communication with proven data continuity;

(4) reconfigurability of the sampling channels for flexible LAST implementation.

The state-of-the-art LAST DAQ systems can be conceptually categorized as raw signal sampling and on-chip preprocessed signal sampling. The raw signal sampling with fully parallel scheme is the most straightforward method that maximally preserves both the temporal information and full spectral information. Its implementation demands an enormous data throughput, which can overload the real-time front/back-end data communication and violates the data continuity. On-board data storage in memories is possible [12]. However, it will easily overflow SDRAM in a few seconds of measurement.

To lower the data throughput for high-speed, real-time and continuous DAQ of LAST measurements, recent effort has been made by implementing various demodulation algorithms on embedded platforms. Most are implemented on a field programmable gate array (FPGAs), which has been widely adopted for industrial signal conditioning [13] and acceleration of image processing [14]. Recent efforts have been made on down sampling the raw transmission signal within a wavelength scan to a few samples, for example, by extracting the peak of each harmonic shown in Fig. 1 (a), via an on-chip neural network based peak extractor [15]. However, the extracted peaks cannot maintain spectral integrity since they are unable to indicate the absorbance lineshape [10], which is an important chemo-physical filter for noise rejection. To avoid degradation of the spectral integrity, accumulator-based digital lock-in amplifiers (DLIA) were developed [16], [17] to down sample the raw transmission signal and maintain the lineshape information. By channel-multiplexing at the modulation frequency, an accumulator-based DLIA has been recently demonstrated with a microsecond-level interval between the neighboring channels [16], as shown in Fig. 1 (b). This is cost-effective in terms of hardware resource for multi-channel DAQ with a single analog-to-digital converter (ADC). However, its implementation requires very high modulation-to-scan frequency ratio (f_m/f_s), since (a) the spectral samples can only be demodulated from an integer number of modulation periods and (b) all the multiplexed channels equally share the demodulated samples. These fundamental limits the scan frequency and thus the image rate up to a few hundred Hz.

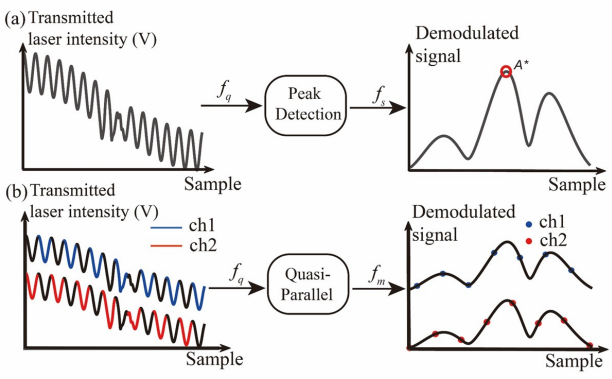

Fig. 1. Schematic of on-chip pre-processing DAQ schemes for (a) peak-detection and (b) quasi-parallel (QP).

To address the above-mentioned challenges, we develop an FPGA-accelerated distributed DAQ system for high-speed LAST imaging with well-maintained spectral information. The developed system is demonstrated experimentally for streaming real-time LAST measurement data between the front and back ends at kHz-level temporal resolution. Distributed deployment of the sensing system also facilitates large-scale industrial implementation of LAST, e.g., visualization of full-size gas turbine exhaust [18] and power-plant boilers [19].

The significance contribution as well as the novelty of the work covers:

1) A novel online DLIA aided by the cascaded integrator-comb (CIC) filter, that is superior to the state-of-art methods in terms of maintaining the spectral information integrity, is designed and implemented on the FPGA. The FPGA-accelerated implementation enables kHz-level and continuous LAST imaging that offers better insight of the dynamics of industrial reactive flowfields.

2) A new laser scan scheme, i.e., semi-scan multiplexing (SSM), is proposed. By utilizing the laser absorption in both crest and trough semi periods of a sinusoidal laser wavelength scan, the LAST imaging rate is maximized at a given wavelength scan frequency. The proposed SSM scheme also maintains strong synchrony and consistency of neighboring-channel DAQ.

3) Customized data encapsulation and de-encapsulation algorithms are developed to check the data continuity between the front/back-end data communication. This implementation facilitates well time stamping between the measurement data with the industrial processes.

4) The Ethernet-networked star topology is introduced for distributed deployment of the DAQ hubs. The independence of each DAQ hub also offers great flexibility to reconfigure the LAST system with increased number of measurement channels.

The rest of the paper is organized as follows. Section II introduces the spectroscopic fundamentals, the proposed SSM scheme and the CIC filter-aided online DLIA. Section III describes the FPGA hardware and firmware design as well as the implementation of the proposed principles and the data encapsulation. Section IV validates the proposed design with a proof-of-concept combustion experiment. The paper is concluded in Section V.

II. Principle of Design

A. Background of WMS

The fundamentals of WMS and its implementation of ratio thermometry have been detailed in [10], [20]. Two laser ab-

sorption transition lines [10], whose wavenumbers are centered at v_1 and v_2, are adopted and thus the corresponding two laser diodes are frequency division multiplexed (FDM) [20], [21] shown in Fig. 2. The lasers are driven by the injected current with the same scan frequency f_s, and different modulation frequencies f_{m1} and f_{m2}, respectively. The laser wavenumber for transition line l (l = 1, 2), $\mu_{v_l}(t)$, is expressed as the superposition of wavenumber scan $\mu_{l,s}(t)$ and modulation $\mu_{l,m}(t)$:

$$\mu_{v_l}(t) = \mu_{l,s}(t) + \mu_{l,m}(t) \tag{1}$$

Accompanied by the wavenumber modulation, the laser incident intensity for transition line l, $I_0^{v_l}(t)$, is also the superposition of scan intensity $I_0^{s_l}(t)$ and modulation intensities $I_0^{m_l}(t)$:

$$I_0^{v_l}(t) = I_0^{s_l}(t) + I_0^{m_l}(t) \tag{2}$$

Coupled by a fiber coupler, the FDM incident laser intensity $I_0(t)$ is:

$$I_0(t) = \sum_{l=1}^{2} I_0^{v_l}(t) \tag{3}$$

For simplicity, subscript l will be eliminated afterwards when working on either of the two transitions.

The incident laser signal is split into N beams. For the i-th beam (i = 1, 2, ..., N), the $I_0(t)$ is absorbed by the target gas molecule. The absorption process is modelled using Beer-Lambert's law, which describes the relationship between the transmitted laser intensity $I_{t,i}(t)$, incident intensity $I_{0,i}(t)$ as well as the absorbance [10]:

$$I_{t,i}(t) = I_{0,i}(t)e^{-\alpha_i[\mu_v(t)]} \tag{4}$$

$$\alpha_i[\mu_v(t)] = \phi[\mu_v(t)] \cdot P_i \cdot S_v(T_i) \cdot X_i \cdot L_i \tag{5}$$

where $\alpha_i[\mu_v(t)]$ is the absorbance, $\phi[\mu_v(t)]$ the line-shape function, $S_v(T_i)$ the transition line strength. P_i, X_i, T_i are the pressure, concentration and temperature of the target gas, respectively. L_i is the absorption path length for the i-th laser beam.

$A_{i,v}$ is defined as the integrated area of the absorbance $\alpha_i[\mu_v(t)]$ over wavenumber $\mu_v(t)$ along the absorption path. As the line shape function is normalized to unit, i.e., $\int_{-\infty}^{+\infty} \phi(\mu)\, d\mu \equiv 1$, it can be expressed as:

$$A_{i,v} = \int \alpha_i(\mu_v) d\mu_v = P_i \cdot S_v(T_i) \cdot X_i \cdot L_i \tag{6}$$

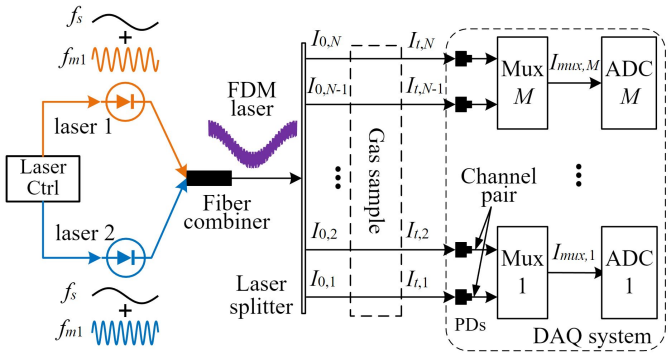

Fig. 2. Diagram of multi-beam digitization of FDM WMS signals using the proposed DAQ system.

Flow parameters distributions, such as temperature and gas concentration, are inferred from $A_{i,v}$. Typically, the first- and second-order harmonics of $I_{t,i}(t)$, i.e., 1f and 2f signals, are demodulated using a DLIA. Then, 1f-normalized WMS-2f signal (WMS-2f/1f) can be calculated by normalizing the 2f signal with the 1f signal. As a result, WMS-2f/1f signal is free from calibration of the laser intensity and laser specific turning characteristics [22]. By least-square fitting the WMS-2f/1f signal, $A_{i,v}$ is extracted and used to infer the absolute flow parameters, such as temperature and gas concentration [23].

B. SSM-WMS scheme for multi-beam LAST sensing

In this subsection, rather than using the full-scan multiplexing [18], [24], the SSM scheme is proposed to maximize the LAST imaging rate at a given f_s. To maintain strong synchrony and consistency of neighboring-channel DAQ, two adjacent beams are bonded as a channel pair shown in Fig. 2 and will be sampled by the same ADC. As a result, the N beams are divided into M (M = N / 2) channel pairs. As illustrated in Fig. 3, the two channels, $I_{t,i}(t)$ and $I_{t,i+1}(t)$, of j-th channel pair, where $j = \lfloor (i+1)/2 \rfloor$ with i an odd integer, are 2-to-1 multiplexed at the crest and trough of the sinusoidal scan, i.e., every semi-scan period. Therefore, both the down and up scan are utilized as two independent measurements. In the k-th laser scan period (k = 1, 2, 3, ...), the multiplexed j-th channel-pair output $I_{mux,j}(t)$ is the sequential of the down

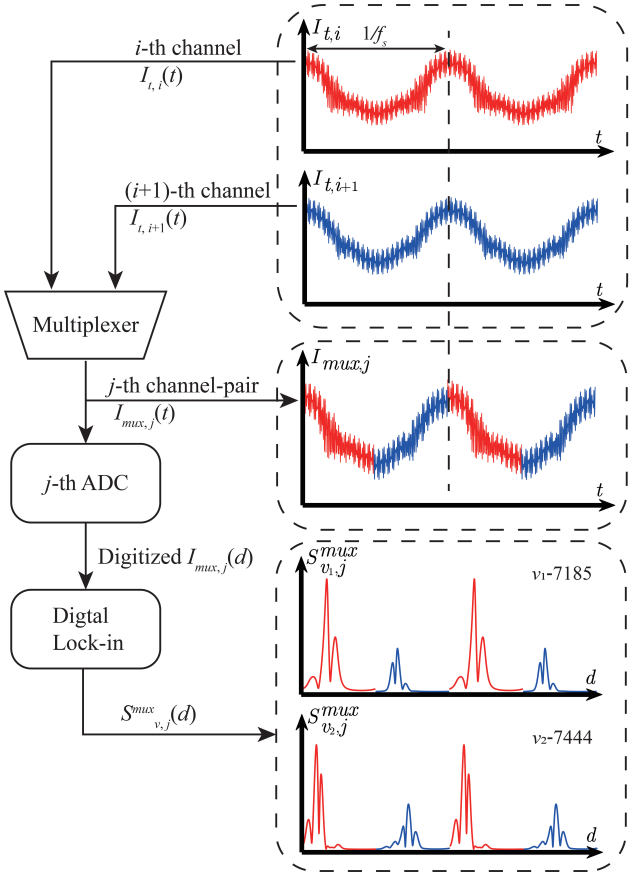

Fig. 3. Flowchart of SSM-WMS scheme for j-th channel-pair.

scan of $I_{t,i}(t)$ and the up scan of $I_{t,i+1}(t)$, which is written as:

$$I_{mux,j}(t) = \begin{cases} I_{t,i}(t), & \frac{(k-1)}{f_s} \le t < \frac{(2k-1)}{2f_s} \\ I_{t,i+1}(t), & \frac{(2k-1)}{2f_s} \le t < \frac{k}{f_s} \end{cases} \quad (7)$$

This multiplexed output is digitized by an ADC with sampling rate f_q and thus the number of wavelength samples P in each scan period is calculated as:

$$P = f_q / f_s \quad (8)$$

Demodulated by the DLIA, WMS-2f/1f for the j-th channel $S_{v,j}^{mux}(d)$, which is also the sequential WMS-2f/1f of the i-th and (i+1)-th laser beams, $S_{v,i}(d)$ and $S_{v,i+1}(d)$, is expressed as :

$$S_{v,j}^{mux}(d) = \begin{cases} S_{v,i}(d), (k-1)P \le d < (k-\frac{1}{2})P \\ S_{v,i+1}(d), (k-\frac{1}{2})P \le d < kP \end{cases} \quad (9)$$

where d is the index of the digitized wavelength samples.

By adopting the above SSM-WMS scheme, the absorption and spectral information of the two laser beams can be sampled using a single ADC channel. As measurement of the two laser beams are implemented sequentially in a scan period, the image frame rate is same as the scan frequency, which is equivalent to a fully parallel DAQ for sawtooth ramp scan with the same scan frequency [18], [21], [24].

C. CIC filter-aided online DLIA technique

We develop a novel DLIA technique, aided by the CIC filter [25], by taking the advantage of down sampling of the raw transmission with well-maintained spectral information. Fig. 4 illustrates the architecture for the proposed demodulator, i.e., a combination of a FPGA-level acceleration and a high (PC)-level of harmonic extraction. Such a separation of the signal flow makes the most use of the efficiency of the two platforms. The former effectively demodulates the multi-channel transmissions accompanied by a spectral information-reserved down sampling, while the latter further denoises the down-sampled data for high-fidelity recovery of the harmonics.

Specifically, the FPGA-accelerated harmonic extraction contains a lock-in module and a CIC filter. Within the former module, the in-phase (I) and quadrature (Q) components of the n^{th}-order harmonic of the digitized j-th channel-pair transmission $I_{mux,j}(d)$ for the transition v, noted as ${}^{I}R_{nf,v,j}$ and ${}^{Q}R_{nf,v,j}$, are isolated by multiplying the I and Q reference signal, i.e., *sin* and *cos* functions with the corresponding frequency nf_m:

$${}^{I}R_{nf,v,j}(d) = I_{mux,j}(d) \cdot \sin(2\pi n f_m \cdot d) \quad (10)$$

$${}^{Q}R_{nf,v,j}(d) = I_{mux,j}(d) \cdot \cos(2\pi n f_m \cdot d) \quad (11)$$

These locked-in components have the same number of samples as the raw transmission $I_{mux,j}(d)$. Then, the CIC filter [25] is introduced, working in two aspects: (a) lowering the data throughput for real-time data transfer; (b) preliminary low-pass filtering of the locked-in components. A single-stage CIC filter contains an integrator, a decimator and a comb filter, with cascade connection. The integrator performs smooth down sampling on ${}^{I}R_{nf,v,j}(d)$ and ${}^{Q}R_{nf,v,j}(d)$, while the overall CIC filter is equivalent to a stable finite-impulse-response (FIR) filter with rectangular impulse response.

The number of the down-sampled WMS-2f/1f wavelength samples P_D within a down or up scan is calculated as:

$$P_D = f_q / (2 * D * f_s) \quad (12)$$

Given the laser is scanned at f_s = 1 kHz and the sampling rate is f_q = 20 MHz, the CIC filter with D = 25 can decrease the number of demodulated wavelength samples from P = 20k to P_D = 400. In comparison with the harmonic peak extraction and accumulator-based DLIA noted in Section I, the CIC filter with configurable D can flexibly satisfy the spectral integrity.

Then, the down-sampled outputs from the CIC filter, noted as ${}^{I}C_{nf,v,j}(d)$ and ${}^{Q}C_{nf,v,j}(d)$, are expressed as recursive forms:

$${}^{Q}C_{nf,v,j}(d) = [{}^{Q}R_{nf,v,j}(d) - {}^{Q}R_{nf,v,j}(d-D)] + {}^{Q}C_{nf,v,j}(d-1) \quad (13)$$

$${}^{I}C_{nf,v,j}(d) = [{}^{I}R_{nf,v,j}(d) - {}^{I}R_{nf,v,j}(d-D)] + {}^{I}C_{nf,v,j}(d-1) \quad (14)$$

Since only addition (subtraction) operations are involved in (12-13), the CIC filter is resource saving and therefore suitable to be implemented on the FPGA. However, the smoothing and comb filters have limited effect on noise elimination. Using the above parameters, Fig. 5 shows the Fast Fourier Transformation (FFT) of the 1f-magnitude $C_{1f,v,j}(d)$, i.e.,

$$C_{1f,v,j}(d) = \sqrt{[{}^{I}C_{1f,v,j}(d)]^2 + [{}^{Q}C_{1f,v,j}(d)]^2} \quad (15)$$

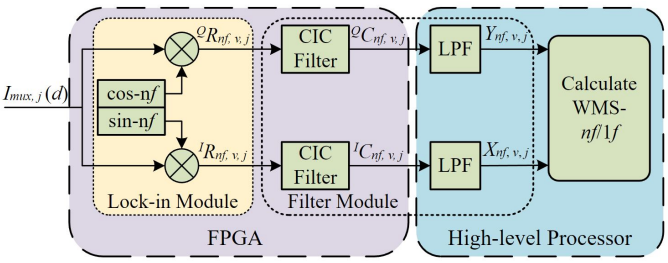

Fig. 4. Flow diagram of CIC filter-aided demodulation of n-th order harmonics.

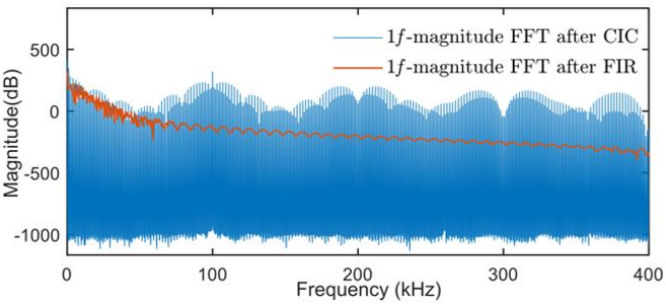

Fig. 5. FFT of 1f-magnitude (f_s = 1 kHz, f_m = 100 kHz and f_q = 20 MHz) output from the CIC filter at D = 25 and 200-order FIR filter, respectively.

The locked-in 1f-harmonics from the CIC filter is dominated by the noise from other frequencies. Therefore, an additional FIR [26] Low Pass Filter (LPF) is implemented on the high-level processor to further remove the noise:

$$X_{nf,v,j}(d) = F[{}^{I}C_{nf,v,j}(d)] \tag{16}$$

$$Y_{nf,v,j}(d) = F[{}^{Q}C_{nf,v,j}(d)] \tag{17}$$

where $X_{nf,v,j}$ and $Y_{nf,v,j}$ are the FIR-low pass filter (LPF) outputs of the I and Q components. $F[\cdot]$ represents the FIR-LPF operation. As shown in Fig. 5, the noise in the 1f-magnitude output from a 200-order FIR filter, for example, is significantly suppressed, enabling $X_{nf,v,j}$ and $Y_{nf,v,j}$ with good SNRs.

Finally, the multiplexed WMS-2f/1f, $S_{v,j}^{mux}$, is calculated as:

$$S_{v,j}^{mux} = \sqrt{\left(\frac{X_{2f,v,j}}{K_{1f,v,j}} - \frac{X_{2f,v,j}^{0}}{K_{1f,v,j}^{0}}\right)^{2} + \left(\frac{Y_{2f,v,j}}{K_{1f,v,j}} - \frac{Y_{2f,v,j}^{0}}{K_{1f,v,j}^{0}}\right)^{2}} \tag{18}$$

$$K_{1f,v,j}^{0} = \sqrt{\left(X_{1f,v,j}^{0}\right)^{2} + \left(Y_{1f,v,j}^{0}\right)^{2}} \tag{19}$$

$$K_{1f,v,j} = \sqrt{\left(X_{1f,v,j}\right)^{2} + \left(Y_{1f,v,j}\right)^{2}} \tag{20}$$

where symbols with superscript '0' correspond to the absorption-free components obtained using the same DLIA.

III. System Implementation

In this section, the proposed DLIA technique is embedded in newly designed FPGA-based multi-channel DAQ electronics. To facilitate data communication from the front end to the back end, a data-encapsulation protocol is proposed and implemented in the FPGA to check the data continuity.

A. Hardware and firmware implementation

As shown in Fig. 6, each developed DAQ hub contains the analogue front-end, FPGA-accelerated signal processing and Ethernet-based data transmission. The analogue front-end has eight channels, i.e., four channel pairs, to make the full use of the Gigabit Ethernet communication bandwidth. The raw analogue input is pre-filtered and amplified by the programmable-gain amplifier (THS7002, Texas Instruments) firstly. According to the SSM scheme, the 8-beam transmitted signals are multiplexed to 4 channel-pair outputs by an 8-to-4 multiplexer (ADG1434, Analog Device) with timing logic controlled from a Cyclone IV FPGA (EP4CE40F29C8, Altera). The multiplexed signal $I_{mux,j}(t)$ is digitized by a 14-bit ADC (AD9251, Analog Device) whose sampling frequency is controlled by the FPGA clock wire *adc_clk* with frequency f_q = 20 MHz. The quantized signal $I_{mux,j}(d)$ is processed in the FPGA according to the proposed online DLIA scheme.

The upper part of Fig. 7 shows the detailed structure of the CIC-aided online DLIA module, in which all the registers are clocked by the ADC clock *adc_clk*. The data flow path is also labeled on Fig. 7. Specifically, I and Q reference signals in (10) and (11) are digitized as 14-bit fixed-point data and stored in the FPGA memory. $I_{mux,j}(d)$ is multiplied by the I and Q reference signals to extract 1f and 2f at the frequency f_m and 2f_m, respectively. As a result, 28-bit fixed-point components ${}^{I}R_{1f,v,j}$, ${}^{Q}R_{1f,v,j}$, ${}^{I}R_{2f,v,j}$ and ${}^{Q}R_{2f,v,j}$ are produced for each transition v, and then streamed into the CIC filter described in (13) and (14). According to (13) and (14), the width of the CIC filter output Bout is calculated by:

$$B_{out} = \lfloor B_{in} + \log_2(D) \rfloor \tag{21}$$

where B_{in} is the CIC filter input data width, i.e., 28 in this case. By setting the decimation factor D = 25, the four components output from the CIC filter, ${}^{I}C_{1f,v,j}$, ${}^{Q}C_{1f,v,j}$, ${}^{I}C_{2f,v,j}$ and ${}^{Q}C_{2f,v,j}$, have 32-bit data width with f_q/D = 800 kSps throughput for each component. It is notable that the decimation factor D is reconfigurable and can be optimized to reach the trade-off between the spectral integrity and maximum usage of Gigabit Ethernet bandwidth. For each DAQ hub, 4 parallel channel pairs with two transitions generate the total data throughput of 819.2 Mbps (4 channel pairs × 32 bits/S × 0.8 M/s × 4 components × 2 transitions). These data will be encapsulated according to the format described in the next subsection and transferred to the data transmission module, in which the User Datagram Protocol (UDP) is realized for real-time data transmission through Gigabit Ethernet. The data

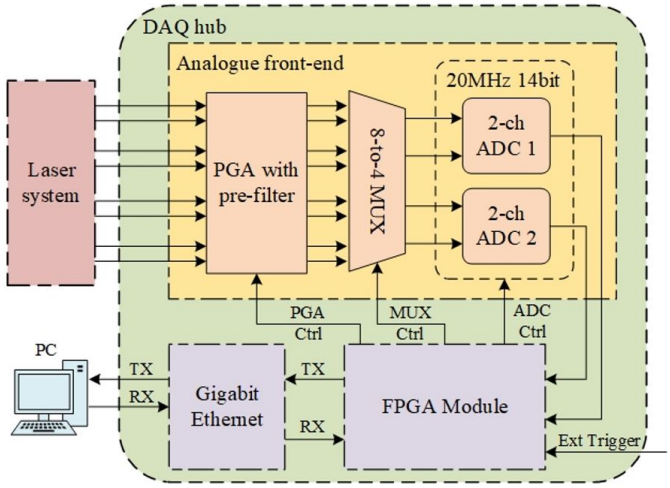

Fig. 6. Schematic of the analogue front-end, FPGA central processor and the Gigabit Ethernet transmission.

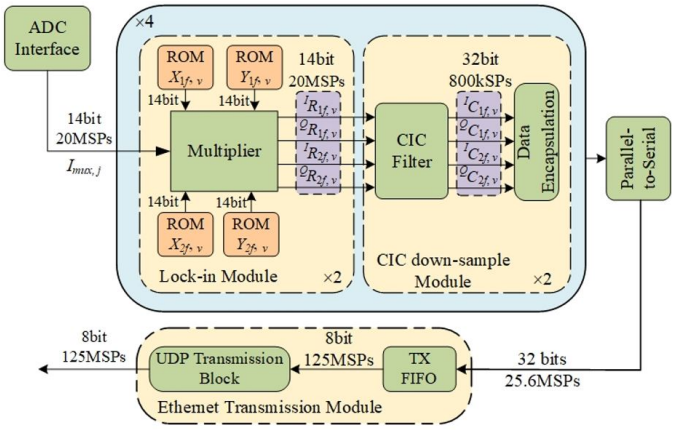

Fig. 7. Data flow diagram for j-th channel-pair output of transition v in FPGA.

transmission is working at a different clock domain, i.e., *gmii_clk* at 125 MHz, and hence a First In, First Out (FIFO) buffer is used to connect the two clock domains.

The FPGA firmware is coded by the hardware description language Verilog, synthesized and implemented using the Quartus Prime 18.1. The firmware performance is evaluated in two aspects, i.e., the resource usage and the timing performance. Specifically, the usage of logic elements, registers, IO pins and 9-bit multipliers is listed in TABLE I as well as the occupation percentage of the total available resources. The resource usage for DLIA purely by FIR LPF [26] is also listed for comparison. The result shows that the developed FPGA firmware is cost-effective and resource-saving as all the hardware resources usage is below 30%. On the contrary, if the DLIA is realized purely FIR, we require extreme large FPGA resources, which far exceed the available resources and are not implementable for the FPGA. Only synthesis is done for the FIR DLIA due to significant excess of hardware resources.

The timing performance is evaluated on the two clocks, i.e., *adc_clk* and *gmii_clk* from ADC sampling and ethernet transmission respectively. As the most critical timing parameter, the setup and hold time slack of each clock, on the worst-case timing path are evaluated. The maximum clock frequency $F_{\max}$ is also calculated according to the worst-case timing path delay. As illustrated in TABLE II, in the worst-case timing path, the time slacks of those two clocks are positive in both setup and hold scenarios, indicating all timing requirements are met. Accordingly, the calculated maximum running frequency $F_{\max}$ of *adc_clk* and *gmii_clk* are 81.17 MHz and 144.59 MHz, which are higher than their target working frequencies of 20 MHz and 125 MHz, respectively.

In a LAST system, the above hardware and firmware configuration are extended to multiple DAQ hubs for the ease of multi-channel reconfiguration. The multiple DAQ hubs are star networked via an Ethernet switch. An external trigger signal is used to synchronize all the hubs with the laser-driving signal.

TABLE I
FPGA RESOURCES COMPARED BETWEEN CIC AND FIR DLIAS

	CIC DLIA Usage/Total (%)	**Pure FIR DLIA Usage/Total (%)**
Logic Elements	4392/39600 (8.36%)	5029k/39600 (12700%)
Registers	2468	5082k
IO Pins	125/533 (23%)	125/533 (23%)
Memory Bits	191k/1161k (16%)	191k/1161k (16%)
9-bit Multiplier	64/232 (28%)	42496/232 (18317%)

TABLE II
TIMING PERFORMANCE EVALUATION OF THE DESIGNED FPGA FIRMWARE

Clock / **Item**	**ADC Sampling** *adc_clk*	**Data Transmission** *gmii_clk*
Setup time Slack (ns)	37.527	1.084
Hold time Slack (ns)	0.149	0.178
Target F (MHz)	20	125
$F_{\max}$ (MHz)	80.17	144.59
Data Delay	12.372	6.485

B. Data encapsulation and continuity check

Data continuity is essential for a LAST DAQ system, ensuring (a) the images are reconstructed at a fixed frame rate

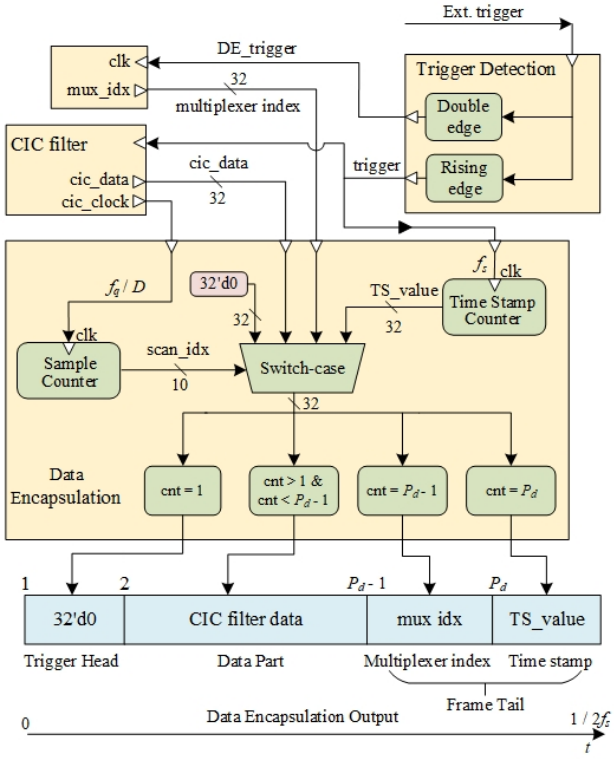

Fig. 8. Schematic design of the data-encapsulation protocol in FPGA.

Algorithm 1: Data continuity checking and continuous signal extraction from the encapsulated data

Input: Number of lock-in components samples per semi-scan P_d, number of parallel lock-in components N_p, encapsulated measured data $\boldsymbol{S}$
Output: Data loss index set $\boldsymbol{I}$, number of discontinuity q and valid continuous data $\boldsymbol{V}$
Initialize: Empty $\boldsymbol{V}$ and $\boldsymbol{I}$, $q \leftarrow 0$, ts_cur $\leftarrow 0$, ts_prev $\leftarrow 0$, $i \leftarrow 0$
$L \leftarrow P_d \times N_p$, $F \leftarrow$ length of $\boldsymbol{S}$
Locate the start of trigger:
for k in {1, 2, …, F} **do**
  if $\boldsymbol{S}(k)$ is 0 **and** $\boldsymbol{S}(k+1)$ is not 0 **then**
    $\boldsymbol{S} \leftarrow \{\boldsymbol{S}(k-31), \boldsymbol{S}(k-30), \ldots, \boldsymbol{S}(F)\}$
    break
Check data continuity:
while $2 \times i \times L < F$ **do**
  ts_prev $\leftarrow$ ts_cur, ts_cur $\leftarrow \boldsymbol{S}(2 \times i \times L + L)$
  mux_down $\leftarrow \boldsymbol{S}(2 \times i \times L + L - N_p)$
  mux_up $\leftarrow \boldsymbol{S}(2 \times (i+1) \times L - N_p)$
  if ts_cur – ts_prev = 1 **and** mux_down =1 **and** mux_down =2 **then**
    $i \leftarrow i + 1$
  else
    $q \leftarrow q + 1$
    $\boldsymbol{I}(q) \leftarrow i$
    for j in $\{2 \times i \times L + 1, 2 \times i \times L + 2, \ldots, F\}$ **do**
      if $\boldsymbol{S}(j : j+31) = \boldsymbol{0}$ **and** $\boldsymbol{S}(j + L - N_p) = 1$ **then**
        remove $\{\boldsymbol{S}(2 \times i \times L + 1), \ldots, \boldsymbol{S}(j-1)\}$
        $F \leftarrow$ length of $\boldsymbol{S}$
        break
$\boldsymbol{V} \leftarrow \boldsymbol{S}$

and (b) each single frame is reconstructed using the projection data sampled from all the laser beams. However, if data discontinuity happens, it is critical to locate the breaking point and the lost period(s). In this case, the remaining measurements can be temporally aligned with the reactive process of the target flow fields. In this subsection, the CIC down-sampled data is encapsulated in the FPGA with a customized protocol, which facilitates the check of data continuity.

In general, the wavelength scan could cover the non-absorption regions [27]. These regions, corresponding to the head and tail of each CIC down-sampled component, will be replaced as the indexing information in the encapsulated data shown in Fig. 8. Once the DAQ is triggered, a counter that is clocked by the decimated sampling frequency (f_q/D), will start to count from zero to P_d, indicating the index of each down (up) scan. The encapsulated data is structured by P_d outputs, each with 32-bit width. Concretely, the first output is given by 32-bit zeros at the start of each down (up) scan to indicate the triggered state. The following 2^{nd} to $(P_d-2)^{\text{th}}$ outputs are the wavelength samples of the same indexed CIC down-sampled component. The $(P_d-1)^{\text{th}}$ output is the multiplexing index, which gives "1" for detecting trigger's rising edge (down scan) and "2" for falling edge (up scan). The last output is a time stamp (TS) that indexes the wavelength scan periods. A TS counter counted on the trigger's rising edge is designed to record the indices. Linear increment of the TS value is expected given non-existence of data discontinuity. Given all the 4 CIC down-sampled components of the 2 transitions in the 4 channel pairs, there are 32 encapsulated data generated in parallel per semi scan. The data is serialized and transferred to the back-end host computer.

To realize the de-encapsulation, Algorithm 1 is developed and implemented on the high-level processor to check the data loss. The algorithm is initialized by detecting the first rising edge of the DAQ trigger. For each wavelength scan period, the TS value and the multiplexer index are extracted. If no data is lost, the TS value should be increased by 1 per scan. The down-scan and up-scan multiplexer indices should be 1 and 2, respectively. Otherwise, the algorithm will relocate the trigger indicator, i.e., the 32-bit zeros, for the next wavelength scan period and remove the samples in the latest discontinuous encapsulation(s). The output $\boldsymbol{I}$ records the index of the scan periods when the data discontinuity is observed.

IV. Experiment Validation

A full DAQ system with 4 hubs is developed to sample the projections from a 32-beam LAST optical sensor. In this work, two transitions of water vapor, one of the main combustion products, are selected at ν_1=7185.6 cm^{-1} and ν_2 = 7444.36 cm^{-1} with laser diodes at both wavenumbers available in our lab. The two lasers are scanned at f_s = 1 kHz and modulated at f_{m1} = 100 kHz and f_{m2} = 130 kHz, respectively. The two laser outputs are fiber coupled and split into 32 laser beams. As shown in Fig. 9, the laser beams are arranged at 4 equiangular projection views with 8 parallel beams in each projection view. More details of the beam arrangement can be found in [28]. The target flames in the sensing region are generated by two identical burners with butane-propane mixed fuel. The diameter the burner outlets is 4.8 cm. The 32 laser beams penetrate the target flames at the height of 5.6 cm above the burner outlets and are detected by 32 photodetectors. Finally, the 32-channel transmitted signals are digitized and demodulated by the developed DAQ system. A 10 Gbps Ethernet switch is used to connect the 4 hubs and the host computer in the star topology.

The full DAQ system will be validated from two aspects: (a) the spectral integrity of the down-sampled harmonics measured using the developed FPGA-accelerated DAQ and (b) image reconstruction at 1 kfps and its data continuity to characterize the dynamics temperature distributions of the reactive flows.

Validation (a): The spectral integrity of the down-sampled demodulated signals is examined by spectral fitting of the measured WMS-2f/1f to a reference one [23]. The reference WMS-2f/1f is obtained using the absorbance line-shape and the spectral parameters, e.g., full-width at half maximum, from HITRAN database [29], which gives full spectral integrity of the target transitions. Therefore, a good fitting result indicates a well-maintained spectral integrity in the down-sampled WMS-2f/1f, and thus high-accuracy projection data, i.e., path

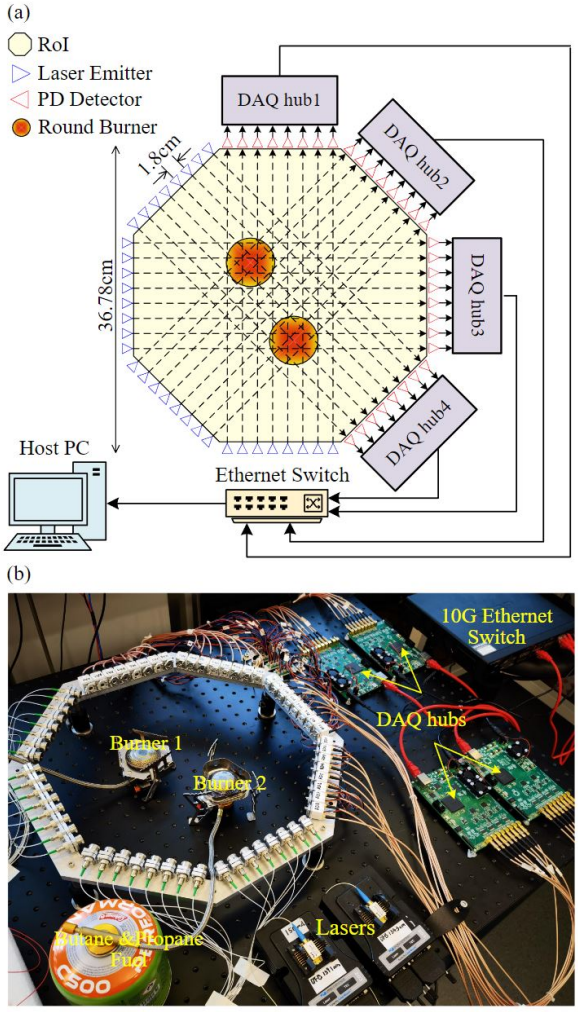

Fig. 9. System implementation of 32-beam LAST experiment. (a) Schematic and (b) picture of the LAST optical sensor and the developed DAQ electronics.

integrated absorbance $A_{v,i}$, extracted from the WMS-2f/1f for the subsequent image reconstruction.

Fig. 10 shows a channel-pair measurement of WMS-2f/1f at the two transitions. Given f_q = 20 MHz and D = 25, P_D is 400. The central 200 out of the 400 WMS-2f/1f wavelength samples are selected to highlight the absorption. By spectrally fitting the down-sampled WMS-2f/1f, the residuals between the measured and fitted signals for all the four cases are smaller than 1%, indicating good agreement between the two signals and thus a well-maintained spectral integrity for the down-sampled signal.

Validation (b): In this experiment, laser transmission is continuously sampled by the proposed DAQ implementation. The first 4 consecutive seconds (s), i.e., 4000 laser scan periods, are selected for detailed analysis. The Algorithm 1 in Section III.B is applied to examine the data continuity of the 4000 sampled periods. The TS values are extracted from the real-time encapsulated data and plotted against the real elapsed time in the experiment. As shown in Fig. 11, the TS value linearly increases as the time elapses, indicating the down-sampled measurements are transferred to the host computer without any breaking points.

In the 4-second experiment, the fuel flow of burner 1 is decreased gradually from 0 to 2$^{\text{nd}}$ second and then increased from 2$^{\text{nd}}$ to 4$^{\text{th}}$ second, while the fuel flow of burner 2 remains stable. The temperature images with 48×48 pixels are reconstructed by CSTNet [30]. Given the imaging rate of 1 kfps, 4,000 frames of temperature images are reconstructed. Fig. 12 shows two representative states of the flames and their cross-sectional temperature reconstructions. Strong consistency exists between the reconstructed temperature distributions and the physical flames. The shapes and radiative intensities of the two flames in Fig. 12 (a) are similar, giving similar temperature profiles and peak values (959 K for flame 1 and 951 K for flame 2) of the two reconstructed hot spots in Fig. 12 (b). Fig. 12 (c) exhibits a much weaker flame generated by burner 1 than that by burner 2, which is also reflected in

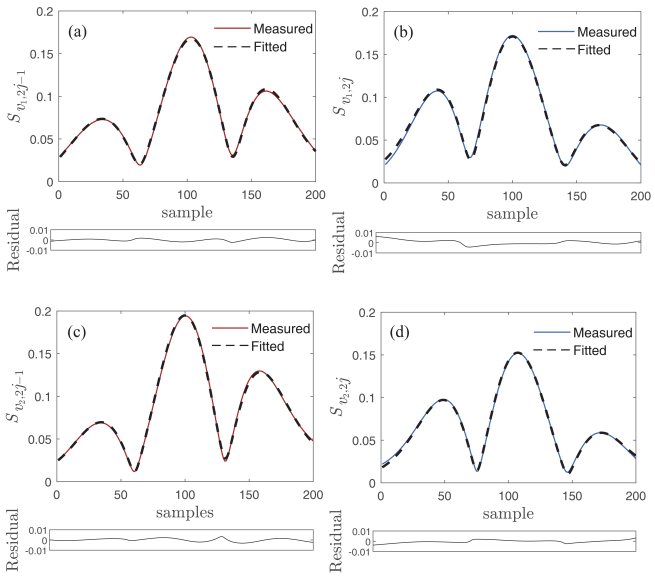

Fig. 10. Example channel-pair measurement and fitted WMS-2f/1f for(a) v_1 at channel 1, (b) v_1 at channel 2,(c) v_2 at channel 1, (d) v_2 at channel 2.

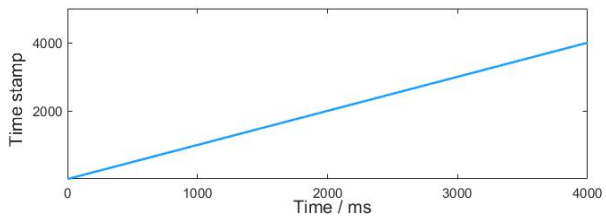

Fig. 11. Continuous time stamps over measurement time (ms).

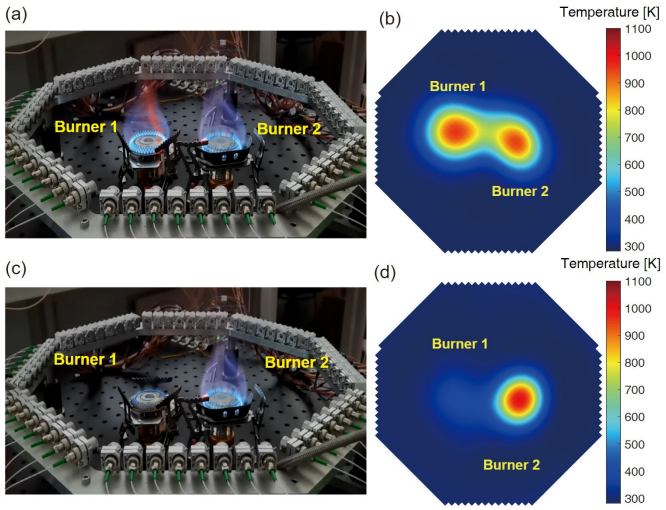

Fig. 12. Pictures of the flame at frames (a) No. 541 and (b) No. 2030, and (c, d) the corresponding reconstructed temperature images.

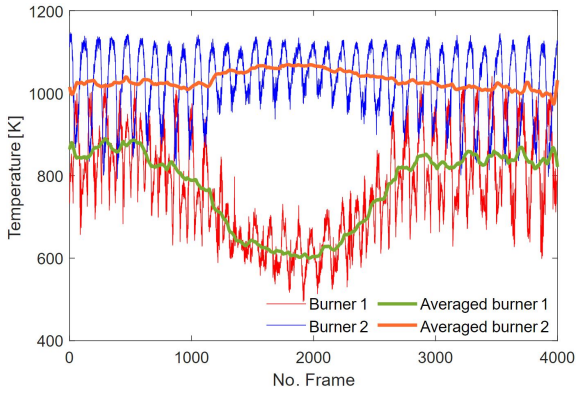

Fig. 13. Extracted time-dependent peak temperature from the two reconstructed hot spots.

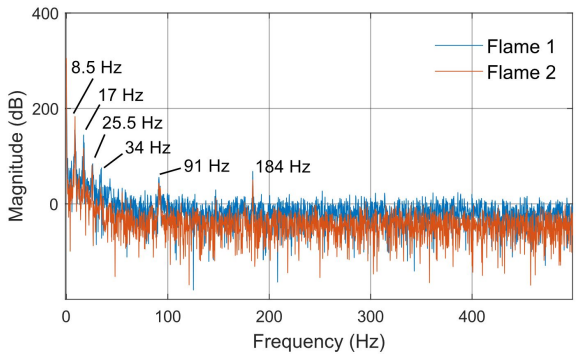

Fig. 14. Frequency analysis of the time-dependent peak temperature value for the two flames.

the reconstructed temperature profiles and peak values (543 K for flame 1 and 990 K for flame 2) of the two hot spots in Fig 12 (d).

In the target flames, regular pulsations and fluctuations can be observed due to their diffusive nature. To quantify the dynamic temperature variations, the peak temperature values and their moving averages of the two flames during the 4-second experiment are obtained. As shown in Fig. 13, the temperature curves of flame 1 clearly present a decreased tendency approximately between frames No. 800 and No. 1700 and then an increased tendency between frames No. 2200 and No. 3000. The temperature curves of flame 2 display a steady state with periodic vibration. Flame pulsation is further analyzed by FFT of the time-dependent peak temperature values of the two flames. As shown in Fig. 14, two flames exhibit similar FFT results. The strongest frequency component locates at 8.5 Hz. The second, third and fourth-order harmonics of fundamental pulsation are also detected at 17 Hz, 25.5 Hz and 34 Hz, respectively. It is noteworthy that the high-frequency pulsation at 91 Hz and 184 Hz, which is not visible by human eyes or the measurement using thermocouples [31], are successfully captured due to the kHz-level temporal resolution of the developed DAQ.

V. Conclusion

A novel FPGA-accelerated distributed DAQ system is designed for dynamic imaging of industrial combustion processes using LAST. The online CIC filter-aided DLI and semi-scan multiplexing schemes are developed and embedded in the FPGA to accelerate the imaging rate to kfps-level, while maintaining adequate spectral integrity and multi-channel sampling synchrony. The measured data is encapsulated with a customized protocol, enabling the check of data continuity during the measurement.

The developed DAQ system is experimentally validated in two steps: First, the measured WMS-$2f/1f$ is spectrally fitted with a residual lower than 1% in comparison with the reference absorbance, indicating good spectral integrity is maintained in the CIC down-sampled signal. Second, dynamic temperature distributions of two diffusive flames are reconstructed at 1 kfps, which agrees well with the real flame features. The groundbreaking temporal resolution enables fine characterization of the flame turbulences. Facilitated by the reconfigurable design concept, the DAQ system can be extended to more channels when applying to large-scale industrial combustion diagnosis.

References

[1] X. Kong and Z. Ge, "Deep learning of latent variable models for industrial process monitoring," *IEEE Transactions on Industrial Informatics*, vol. 18, no. 10, pp. 6778–6788, 2022.

[2] L. Yao and Z. Ge, "Industrial big data modeling and monitoring framework for plant-wide processes," *IEEE Transactions on Industrial Informatics*, vol. 17, no. 9, pp. 6399–6408, 2021.

[3] S. Bao, H. Yan, Q. Chi, Z. Pang, and Y. Sun, "FPGA-based reconfigurable data acquisition system for industrial sensors," *IEEE Transactions on Industrial Informatics*, vol. 13, no. 4, pp. 1503–1512, 2017.

[4] M. Wang, *Industrial tomography: systems and applications*. Woodhead Publishing, 2015.

[5] S. Liu, Y. Huang, H. Wu, C. Tan, and J. Jia, "Efficient multitask structure-aware sparse bayesian learning for frequency-difference electrical impedance tomography," *IEEE Transactions on Industrial Informatics*, vol. 17, no. 1, pp. 463–472, 2021.

[6] H. Liu, C. Tan, M. Soleimani, and F. Dong, "Transmission/reflection dual-mode ultrasonic tomography using weighted least square-lagrange joint reconstruction," *IEEE Transactions on Industrial Informatics*, pp. 1–9, 2022, doi: 10.1109/TII.2022.3221218 [Early Access].

[7] M. Li, L. Xu, and Z. Cao, "Tdlas tomography system for online imaging and dynamic process playback of temperature and gas mole fraction," *IEEE Transactions on Instrumentation and Measurement*, vol. 71, pp. 1–10, 2022.

[8] H. McCann, P. Wright, K. Daun, S. J. Grauer, C. Liu, and S. Wagner, "Chemical species tomography," in *Industrial Tomography*. Elsevier, 2022, pp. 155–205.

[9] C. Liu and L. Xu, "Laser absorption spectroscopy for combustion diagnosis in reactive flows: A review," *Applied Spectroscopy Reviews*, vol. 54, no. 1, pp. 1–44, 2019.

[10] C. S. Goldenstein, R. M. Spearrin, J. B. Jeffries, and R. K. Hanson, "Infrared laser-absorption sensing for combustion gases," *Progress in Energy and Combustion Science*, vol. 60, pp. 132–176, 2017.

[11] A. Farooq, A. B. Alquaity, M. Raza, E. F. Nasir, S. Yao, and W. Ren, "Laser sensors for energy systems and process industries: Perspectives and directions," *Progress in Energy and Combustion Science*, vol. 91, p. 100997, 2022.

[12] H. Zhang, Z. Cao, W. Zhao, A. Huang, Z. Cai, and L. Xu, "A compact laser absorption spectroscopy tomographic system with short spectral scanning time and adjustable frame rate," *IEEE Transactions on Instrumentation and Measurement*, vol. 69, no. 10, pp. 8226–8237, 2020.

[13] R. Ma, J. Gong, G. Liu, and Q. Hao, "Enabling cognitive pyroelectric infrared sensing: From reconfigurable signal conditioning to sensor mask design," *IEEE Transactions on Industrial Informatics*, vol. 16, no. 7, pp. 4436–4446, 2020.

[14] P. Čížek and J. Faigl, "Real-time fpga-based detection of speeded-up robust features using separable convolution," *IEEE Transactions on Industrial Informatics*, vol. 14, no. 3, pp. 1155–1163, 2018.

[15] A. Huang, Z. Cao, C. Wang, J. Wen, F. Lu, and L. Xu, "An fpga-based on-chip neural network for tdlas tomography in dynamic flames," *IEEE Transactions on Instrumentation and Measurement*, vol. 70, pp. 1–11, 2021.

[16] G. Enemali, R. Zhang, H. McCann, and C. Liu, "Cost-effective quasi-parallel sensing instrumentation for industrial chemical species tomography," *IEEE Transactions on Industrial Electronics*, vol. 69, no. 2, pp. 2107–2116, 2022.

[17] E. M. D. Fisher *et al.*, "A custom, high-channel count data acquisition system for chemical species tomography of aero-jet engine exhaust plumes," *IEEE Transactions on Instrumentation and Measurement*, vol. 69, no. 2, pp. 549–558, 2020.

[18] A. Upadhyay *et al.*, "Tomographic imaging of carbon dioxide in the exhaust plume of large commercial aero-engines," *Applied optics*, vol. 61, no. 28, pp. 8540–8552, 2022.

[19] Y. Deguchi *et al.*, "Applications of laser diagnostics to thermal power plants and engines," *Applied Thermal Engineering*, vol. 73, no. 2, pp. 1453–1464, 2014.

[20] W. Wei, W. Y. Peng, Y. Wang, J. Shao, C. L. Strand, and R. K. Hanson, "Two-color frequency-multiplexed ims technique for gas thermometry at elevated pressures," *Applied Physics B*, vol. 126, no. 3, p. 51, 2020.

[21] A. Huang, Z. Cao, W. Zhao, H. Zhang, and L. Xu, "Frequency-division multiplexing and main peak scanning wms method for tdlas tomography in flame monitoring," *IEEE Transactions on Instrumentation and Measurement*, vol. 69, no. 11, pp. 9087–9096, 2020.

[22] G. B. Rieker, J. B. Jeffries, and R. K. Hanson, "Calibration-free wavelength-modulation spectroscopy for measurements of gas temperature and concentration in harsh environments," *Applied optics*, vol. 48, no. 29, pp. 5546–5560, 2009.

[23] C. S. Goldenstein, C. L. Strand, I. A. Schultz, K. Sun, J. B. Jeffries, and R. K. Hanson, "Fitting of calibration-free scanned-wavelength-modulation spectroscopy spectra for determination of gas properties and absorption lineshapes," *Applied optics*, vol. 53, no. 3, pp. 356–367, 2014.

[24] C. Liu, Z. Cao, Y. Lin, L. Xu, and H. McCann, "Online cross-sectional monitoring of a swirling flame using tdlas tomography," *IEEE Transactions on Instrumentation and Measurement*, vol. 67, no. 6, pp. 1338–1348, 2018.

[25] G. Li, E. Dong, and W.-h. Ji, "A near-infrared trace co2 detection system based on an 1,580 nm tunable diode laser using a cascaded integrator

comb (cic) filter-assisted wavelength modulation technique and a digital lock-in amplifier," *Frontiers in Physics*, vol. 7, p. 199, 2019.
[26] M. B. Trimale and Chilveri, "A review: Fir filter implementation," in *2017 2nd IEEE International Conference on Recent Trends in Electronics, Information Communication Technology (RTEICT)*, 2017, pp. 137–141.
[27] Y. Ji, K. Duan, Z. Lu, and W. Ren, "Mid-infrared absorption spectroscopic sensor for simultaneous and in-situ measurements of ammonia, water and temperature," *Sensors and Actuators B: Chemical*, vol. 371, p. 132574, 2022.
[28] R. Zhang, J. Si, G. Enemali, Y. Bao, and C. Liu, "Spatially driven chemical species tomography with size-adaptive hybrid meshing scheme," *IEEE Sensors Journal*, vol. 22, no. 13, pp. 12 728–12 737, 2022.
[29] I. E. Gordon *et al.*, "The hitran2020 molecular spectroscopic database," *Journal of quantitative spectroscopy and radiative transfer*, vol. 277, p. 107949, 2022.
[30] Y. Jiang *et al.*, "Cstnet: A dual-branch convolutional neural network for imaging of reactive flows using chemical species tomography," *IEEE Transactions on Neural Networks and Learning Systems*, pp. 1–11, 2022, doi: 10.1109/TNNLS.2022.3157689 [Early Access].
[31] T. Li *et al.*, "Real-time tool wear monitoring using thin-film thermocouple," *Journal of Materials Processing Technology*, vol. 288, p. 116901, 2021.

Jiangnan Xia Jiangnan Xia received the B.Eng. degree (Hons.) in electrical and electronics engineering from University of Edinburgh, U.K., in 2020, and the B.Eng. degree (Hons.) in electrical engineering and automation from North China Electrical Power University, China, in 2020. He is currently pursuing the Ph.D. degree with the Agile Tomography Group, School of Engineering, University of Edinburgh.

His current research interests are focused on embedded system design for data acquisition system, laser absorption spectroscopy and chemical species tomography.

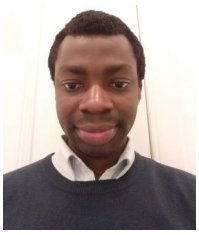

Godwin Enemali Godwin Enemali (Member, IEEE) received the B.Eng. degree (First Class) in electrical and electronics engineering from the University of Agriculture Makurdi, Nigeria, in 2010, and the M.Sc. and Ph.D. degrees in electronics engineering from University of Edinburgh, U.K., in 2014 and 2019, respectively. From 2018 to April 2022, he was a Research Associate with Agile Tomography Group, School of Engineering, University of Edinburgh. Since April 2022, his has been a Lecturer in the Department of Electrical and Electronic Engineering at Glasgow Caledonian University.

His current research interests are on embedded systems, high-speed data acquisition systems, reliable FPGA-based system implementation, laser absorption spectroscopy, and chemical species tomography.

Rui Zhang Rui Zhang received the B.Eng. degree (Hons.) in electronics and electrical engineering with management from University of Edinburgh, U.K., in 2019, and the B.Eng. degree (Hons.) in internet of things engineering from Tianjin University, China, in 2019. She is currently pursuing the Ph.D. degree with the Agile Tomography Group, School of Engineering, University of Edinburgh.

Her current research interest is focused on laser absorption spectroscopic tomography for combustion diagnose.

Yalei Fu is a PhD student supervised by Dr. Chang Liu, within Agile Tomography group, University of Edinburgh. She received her BEng degree in Electronic and Electrical Engineering at University of Edinburgh and started her PhD study in 2020.

Miss Fu's research interests are focusing on LAS tomography and image reconstruction algorithms.

Hugh McCann graduated BSc (1976) and PhD (1980) at the University of Glasgow, UK. After research in high-energy particle physics (1976-86) and ten years at Royal Dutch/Shell, he was appointed Professor of Industrial Tomography (1996-2013) at the University of Manchester, UK, and was Head of the School of Electrical and Electronic Engineering (1999-2002). In 2013, he was appointed Head of the School of Engineering and Professor of Tomographic Imaging at The University of Edinburgh, UK, where he is now Professor Emeritus. Elected a Fellow of the Royal Academy of Engineering (2009) and the Royal Society of Edinburgh (2015), he was appointed Honorary Professor at Beihang University, Beijing, China (2018).

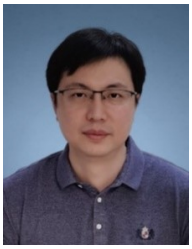

Bing Zhou received the B.Sc. and Ph.D. degrees from the Southeast University, Nanjing, China, in 2002 and 2008, respectively. He is Professor at The Southeast University. His current research interests include NIR/MIR laser absorption spectroscopy (LAS), electrical capacitance tomography (ECT), and their applications to combustion diagnosis and industrial application.

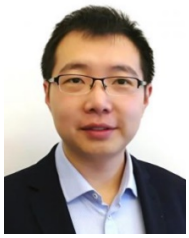

Chang Liu Chang Liu (Senior Member, IEEE) received the B.Sc. degree in automation from Tianjin University, China, in 2010, and the Ph.D. degree in testing, measurement technology, and instrument from Beihang University, China, in 2016.

From April 2016 to January 2018, he was a Post-Doctoral Researcher with the Department of Air Pollution and Environmental Technology, Empa, Swiss Federal Laboratories for Materials Science and Technology, Dübendorf, Switzerland. From February 2018 to July 2023, he has been a Lecturer with the School of Engineering, University of Edinburgh, U.K. He is currently a Senior Lecturer with research interests including NIR/MIR laser absorption spectroscopy, active/passive optical tomography techniques and system design, and their applications to flow-field diagnosis and environmental monitoring.